



Article

# Research on the Relationship Between the Microstructure of Embedded Micro-Agglomerated Particle TBCs and Their Sintering Resistance Based on a Data-Mechanism Hybrid Driving Model

Dongdong Ye <sup>1,2</sup>, Shuheng Xu <sup>1,2</sup>, Zhou Xu <sup>3,\*</sup>, Jiabao Pan <sup>1</sup>, Changdong Yin <sup>3</sup>, Yiwen Wu <sup>4</sup>, Houli Liu <sup>2</sup>, Ting Yang <sup>5,\*</sup> and Jibo Huang <sup>6,\*</sup>

- School of Mechanical and Automotive Engineering, Anhui Polytechnic University, Wuhu 241000, China; ddyecust@ahpu.edu.cn (D.Y.); 2220110152@stu.ahpu.edu.cn (S.X.); panjiabao@ahpu.edu.cn (J.P.)
- <sup>2</sup> School of Artificial Intelligence, Anhui Polytechnic University, Wuhu 241000, China; hlliu@ahpu.edu.cn
- School of Electrical and Automation, Wuhu Institute of Technology, Wuhu 241006, China; 101044@whit.edu.cn
- Institute of Intelligent Manufacturing, Wuhu Institute of Technology, Wuhu 241006, China; 101138@whit.edu.cn
- Inner Mongolia Academy of Science and Technology, Hohhot 010020, China
- School of Materials Science and Engineering, South China University of Technology, Guangzhou 510640, China
- \* Correspondence: 101043@whit.edu.cn (Z.X.); yt19930910@163.com (T.Y.); huangjibo@scut.edu.cn (J.H.)

Abstract: The distribution morphology and density of micro-agglomerated particles are the main microstructural characteristics of embedded micro-agglomerated particle thermal barrier coatings. The study of their effect on the sintering resistance of coatings can help to further improve the service life of thermal barrier coatings. Strain tolerance and thermal insulation performance are important evaluation indicators for the sintering resistance of thermal barrier coatings. In this study, embedded micro-agglomerated particle thermal barrier coatings were prepared by plasma spraying, and the distribution morphology and density of micro-agglomerated particles were analyzed and counted. Different simulation models were established to analyze the compressive stress and thermal stress of the coating, as well as the influence of the microstructure characteristics on the strain tolerance and thermal insulation performance of the coating. A machine learning model was established to evaluate the nonlinear relationship between the microstructure characteristics of the coating and its strain tolerance and thermal insulation performance. The results show that the horizontal angle of the micro-agglomerated particles in the coating has the most significant effect on the sintering resistance and is predicted using the PSO-SVM machine learning model. The predicted effects are the most important, and the coefficients of determination for strain tolerance and thermal insulation are as high as 0.988 and 0.945, respectively, indicating a strong correlation between the predicted and actual values. This research technique used experimental research-simulation computation-machine learning can be used to optimize the microstructure of coatings and guide the preparation of highperformance thermal barrier coatings.

**Keywords:** thermal barrier coatings; sintering resistance; finite element analysis; machine learning



Academic Editor: Alessandro Latini

Received: 4 December 2024 Revised: 24 December 2024 Accepted: 28 December 2024 Published: 31 December 2024

Citation: Ye, D.; Xu, S.; Xu, Z.; Pan, J.; Yin, C.; Wu, Y.; Liu, H.; Yang, T.; Huang, J. Research on the Relationship Between the Microstructure of Embedded Micro-Agglomerated Particle TBCs and Their Sintering Resistance Based on a Data-Mechanism Hybrid Driving Model. Coatings 2025, 15, 24. https://doi.org/10.3390/coatings15010024

Copyright: © 2024 by the authors. Licensee MDPI, Basel, Switzerland. This article is an open access article distributed under the terms and conditions of the Creative Commons Attribution (CC BY) license (https://creativecommons.org/licenses/by/4.0/).

Coatings 2025, 15, 24 2 of 19

# 1. Introduction

Thermal barrier coatings (TBCs) are functional coatings that are widely used on hot-end components, such as aero-engine turbine blades. The use of TBCs increases the operating temperature of aero-turbine engines and improves their efficiency and performance of turbine engines [1–7]. The microstructure of TBCs affects the strain tolerance and thermal insulation of the coating, and strain tolerance and thermal insulation are two important performance indicators for evaluating the sintering resistance of TBCs [8–12]. Therefore, a study of the nonlinear relationship between different microstructural features of TBCs and their strain tolerance and thermal insulation performance is of great significance in establishing a model of the relationship between microstructural characteristics and the service performance of the two types, providing the basis for further improving the service performance of the thermal barrier coatings.

Atmospheric plasma spraying (APS) is the primary method for preparing TBCs. It offers a high deposition efficiency, a simple process, and a fast preparation rate. APS TBCs typically exhibit a layered structure with numerous pores and microcracks between the particles of the coated layer [13]. It was these pores and microcracks that contributed to TBCs's low elastic modulus and thermal conductivity, enabling APS TBCs to have high strain tolerance and thermal insulation performance [4,14–16]. However, in a longterm high-temperature operating environment, some of the tiny pores and microcracks of TBCs will inevitably heal, resulting in sintering. Sintering will lead to a decrease in the service life of TBCs [17,18]. In order to further improve the sintering resistance of APS TBCs. Based on plasma spraying, researchers have proposed a new strategy for TBC preparation by introducing second phase micro-agglomerated particles (MAP); this enabled the incorporation of MAP within conventional TBC substrates, and the novel thermal barrier coatings obtained by this method are called embedded micro-agglomerated particle TBCs (EMAP TBCs). Due to the unique pore structure of the MAP embedded in the coating, EMAP TBCs are highly sintering resistant compared to conventional TBCs [12,19]. During the plasma spraying process, the microstructure of EMPA TBCs can be changed by varying the spraying parameters, which, in turn, changes the performance of the sintering resistance of the TBCs. Therefore, the influence of the microstructure characteristics of EMAP TBCs on the sintering resistance of the coating is studied, which provides a reference for further improving the sintering resistance of EMAP TBCs. Combining experimental data to establish a reasonable mathematical model or finite element model and explore the correlation between the coating microstructure and its sintering resistance is a more conventional study method. Cocks [20] and Cipitria et al. [21] established the block model and constitutive theory of TBCs sintering based on the principle of material diffusion during sintering and the microstructure characteristics of atmospheric plasma TBCs. The evolution of the microstructure, elastic modulus, and thermal conductivity of the coating caused by sintering was predicted. The evolution of the microstructure, elastic modulus, and thermal conductivity of the coating due to sintering was predicted. Li et al. [22] established an image-only lamellar sintering model by varying the sintering neck and lamellar bonding rate at each stage of sintering and discussed the influence law of sintering on the apparent elastic modulus and thermal conductivity of the coating. Using real SEM images, Fartash et al. [23] used cohesion modeling and finite element analysis to simulate interfacial delamination and study the effect of the pore microstructure of the coating on its interfacial damage. However, conventional methods cannot accurately describe the complex nonlinear relationship between the microstructure of TBCs and their sintering resistance in many cases. Machine learning algorithms have been developed maturely, but further development is needed in the application field of TBC microstructures and their performance. Alkurdi et al. [24] developed a genetic algorithm-enhanced machine learning

Coatings 2025, 15, 24 3 of 19

model to predict the stresses and strains in TBCs under thermal loading conditions, and the predictions were significant. Li R et al. [25] established a hybrid machine learning model of the Elman neural network combined with principal component analysis and whale algorithm for optimization combined with terahertz detection for the measurement of the thickness of TBCs, and its prediction accuracy was high. In this paper, the influence of different microstructure characteristics of EMAP TBCs on their strain tolerance and thermal insulation performance was studied in depth, and a mechanism-data hybrid model based on experimental research, simulation calculation, and machine learning is proposed to evaluate the nonlinear relationship between the microstructure of EMAP TBCs and their strain tolerance and thermal insulation performance, which provides an important reference value for further improving the sintering resistance of TBCs. In this study, EMAP TBCs were prepared using an improved plasma spraying process, their microstructure characteristics were characterized by scanning electron microscopy, and the SEM map of the coating microstructure was analyzed by imaging software. A finite element simulation model was established on the basis of the experimentally prepared EMAP TBC microstructures to investigate the influence of different distributed structural features of MAP on the strain tolerance and thermal insulation performance of the coatings by changing the coating microstructural features. Through the orthogonal test combined with the method of range analysis, the influence of different microstructure characteristic factors on the performance of sintering resistance of the coating was analyzed. Based on the microstructure data of the coating and the compressive stress and thermal stress data calculated by finite element simulation, a machine learning model was established to construct an evaluation relationship model between the microstructure characteristics of the coating and its strain tolerance and thermal insulation performance.

# 2. Experiments and Methods

### 2.1. Preparation and Characterization of TBCs

In this study, EMAP TBCs were prepared using an atmospheric plasma spraying system. As shown in Figure 1, unlike conventional TBCs prepared by a single powder feeder, EMAP TBCs add a second powder feeder to transport MAP based on the conventional powder feeding method (shown in Figure 1b). The second powder feeder is 35 mm away from the first powder feeder, and the first powder feeder is located in the high-temperature area of plasma flame flow to ensure that the 8 wt% Yttria-stabilized Zirconia (8YSZ) powder is fully melted to form a dense conventional coating. The second powder feeder is located in the low-temperature region of the plasma flame flow so that the MAP retains its porous microstructure after slight sintering. The second phase MAP is embedded in the conventional coating of the first phase after plasma spraying, thereby forming EMAP TBCs. In particular, MAP is formed by the agglomeration of several 1–5  $\mu$ m 8YSZ powder particles, and the MAP still maintains a loose and porous microstructure after being slightly sintered by atmospheric plasma. In this study, EMAP TBCs were prepared using 8YSZ powder particles.

As shown in Figure 2, the 10–45 µm 8YSZ powder particles (provided by Beijing Sansprei New Materials Co., Ltd., Beijing, China) are spherical after spheroidization, and the 8YSZ powder particles have excellent thermal insulation properties and a relatively stable structure.

EMAP TBC samples were prepared using a commercial atmospheric plasma spraying system (APS-200). A disc-shaped nickel-iron alloy, Incoloy 738, with a diameter of 30 mm and a thickness of 5 mm was used as the substrate. Firstly, the alloy substrate was sand-blasted. Then, a NiCrAlY bonding layer with a thickness of about 200  $\mu$ m was prepared by atmospheric plasma spraying on the surface of the sandblasted nickel-based alloy substrate.

Coatings 2025, 15, 24 4 of 19

The APS-200 plasma spraying system used argon (Ar) as the main plasma gas, hydrogen ( $H_2$ ) as the auxiliary gas to generate the plasma flame, and nitrogen ( $N_2$ ) as the powder carrier gas. During the spraying process, the pressure of the main gas and the auxiliary gas is controlled at 0.4 and 0.25 MPa, respectively. The flow rate of argon is controlled at 45 L/min. The power of plasma spraying is controlled by adjusting the hydrogen flow rate and current. The NiCrAIY bonding layer was prepared by controlling the arc power at 30 kW, gun movement rate at 500 mm/s, and spraying distance at 100 mm. The YSZ ceramic layer was prepared using two powder feeders to feed the powder separately, and the specific process parameters are shown in Table 1.

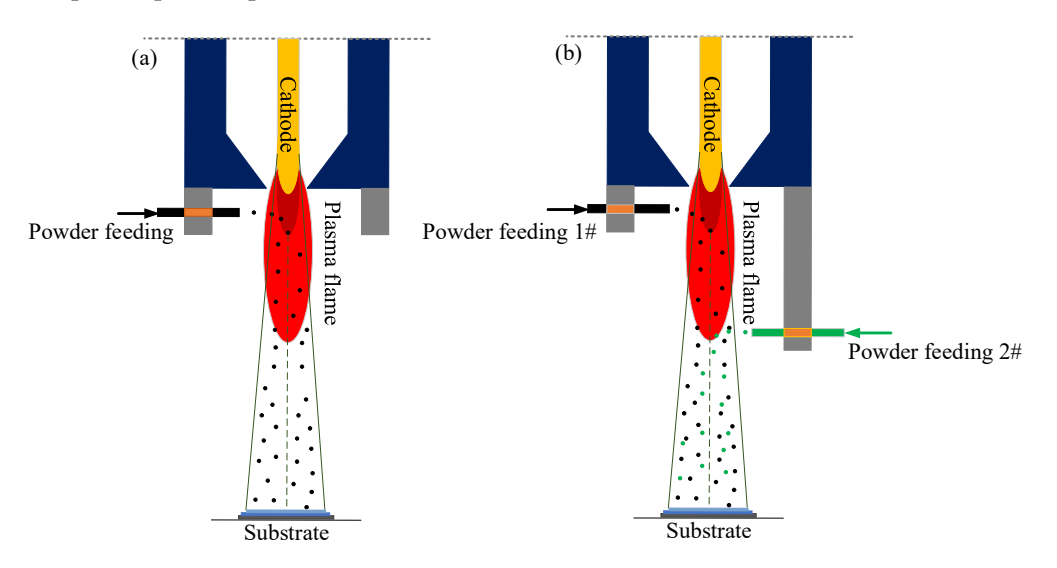


**Figure 1.** Schematic diagram of the coating preparation process. (a) APS preparation process of conventional YSZ thermal barrier coating; (b) Improved APS process for EMAP thermal barrier coating [12].

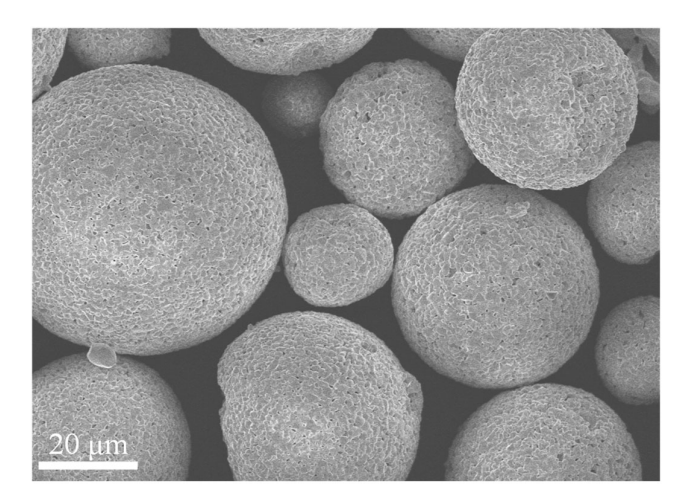


Figure 2. SEM image of the 8YSZ powder.

Table 1. Plasma spraying process parameters.

Parameter	Numerical Value
Gun movement rate	500 mm/s
Spray gun power	39.6 kW
Spraying distance	100 mm
First powder feeder rate\Carrier gas flow rate	$12 \text{ g/min} \setminus 2.0 \text{ L/min}$
Second powder feeder rate\Carrying gas flow rate	$16 \text{ g/min} \setminus 3.0 \text{ L/min}$

Coatings 2025, 15, 24 5 of 19

In order to determine the stability of the process, we prepared eight samples and analyzed the microstructure of these samples. Wire cutting technology (XKG200, Suzhou Hualong Dajin Electro-Machining Co., Ltd., Suzhou, China) is used to accurately cut the thermal barrier coating samples. An ultrasonic cleaning machine is used to clean and remove pollutants. The cross-section of the sample was polished with 1000–3000 mesh sandpaper and then polished. Scanning electron microscopy (SEM, Japan Hitachi S-4800, Tokyo, Japan) was used to characterize the microstructure of the EMAP TBCs cross-section; the SEM voltage was set to 15 kV, the magnification was adjusted to 500–3500, and at least five sets of SEM images of different regions were taken for statistical analysis under the combination of each set of process parameters.

# 2.2. Finite Element Modeling

In this study, finite element simulation was used to explore the effects of different EMAP TBC microstructure characteristics on the strain tolerance and thermal insulation performance of the coating. As shown in Figure 3a, according to the SEM image of the coating cross-section, the EMAP TBCs include a conventional coating matrix. The porous MAP is embedded inside the coating in a form similar to an ellipse. The microstructure characteristics of EMAP TBCs mainly include the MAP density, horizontal angle, ovality, vertical distance, and top distance. Therefore, as shown in Figure 3b, the SIMULIA Abaqus (Version 2021 FP.CFA.2132) software was used to build the finite element model, a coating substrate with a thickness of 200 µm was created, and the MAP was made equivalent to an ideal ellipse embedded in the coating substrate. After experimental analysis and statistics, the density of MAP was set to 20%–30%, the top distance was set to 8–48 µm, the vertical distance was set to  $18-35 \mu m$ , the horizontal angle was set to  $0-170^{\circ}$ , and ovality was set to 0.4–1.0, and specific analysis of coating microstructural features is shown in Section 3.1. The model contains 13,845 meshes, plane strain, and coupled temperaturedisplacement elements that were used to investigate the strain tolerance performance and thermal insulation performance of EMAP TBCs. When the material physical parameters are determined, it is difficult to obtain accurate material physical parameters of the EMAP TBCs matrix and MAP through experimental measurements. From the coating preparation process, it can be seen that the EMAP TBCs matrix preparation process is consistent with the conventional coating, so the material parameters of the matrix part of EMAP TBCs were set to be the same as those of the conventional coating. MAP was set to a lower elastic modulus and thermal conductivity due to its porous microstructural morphology.

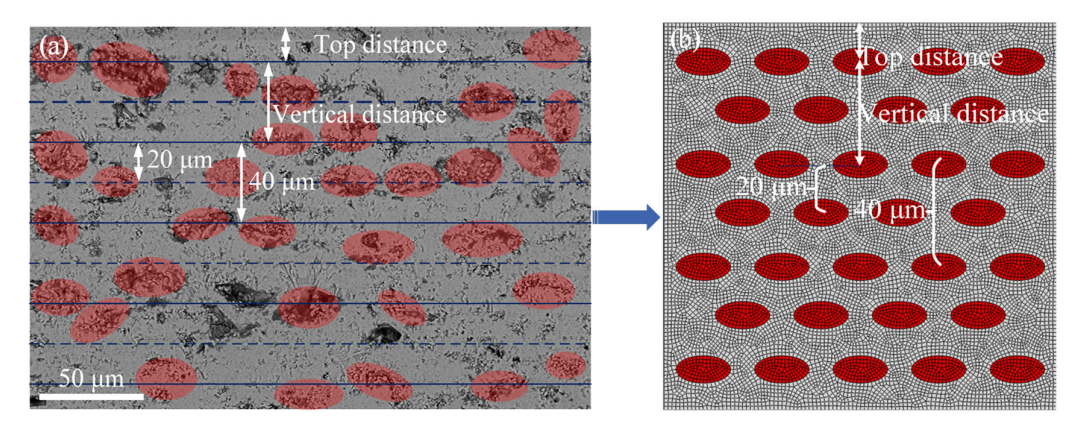


**Figure 3.** Finite element calculation model based on actual microstructure characteristics. (a) EMAP TBCs microstructure characterization diagram; (b) EMAP TBCs finite element simulation model diagram.

In this study, the compressive stress and thermal stress distributions of the coatings corresponding to different EMAP TBCs microstructural features were calculated using

Coatings 2025, 15, 24 6 of 19

> finite element simulation for EMAP TBCs under indentation load and temperature load, respectively, to analyze the effects of different EMAP TBCs microstructural features on the strain tolerance and thermal insulation performance of EMAP TBCs. As shown in Figure 4a, a spherical indenter was used to apply an indentation load of 2 μm to the coating at the upper boundary of the model, and the lower boundary was fixed during the finite element calculation. As shown in Figure 4b, a temperature load of 1100 °C was applied to the upper boundary of the coating finite element simulation model, and the lower boundary was fixed.

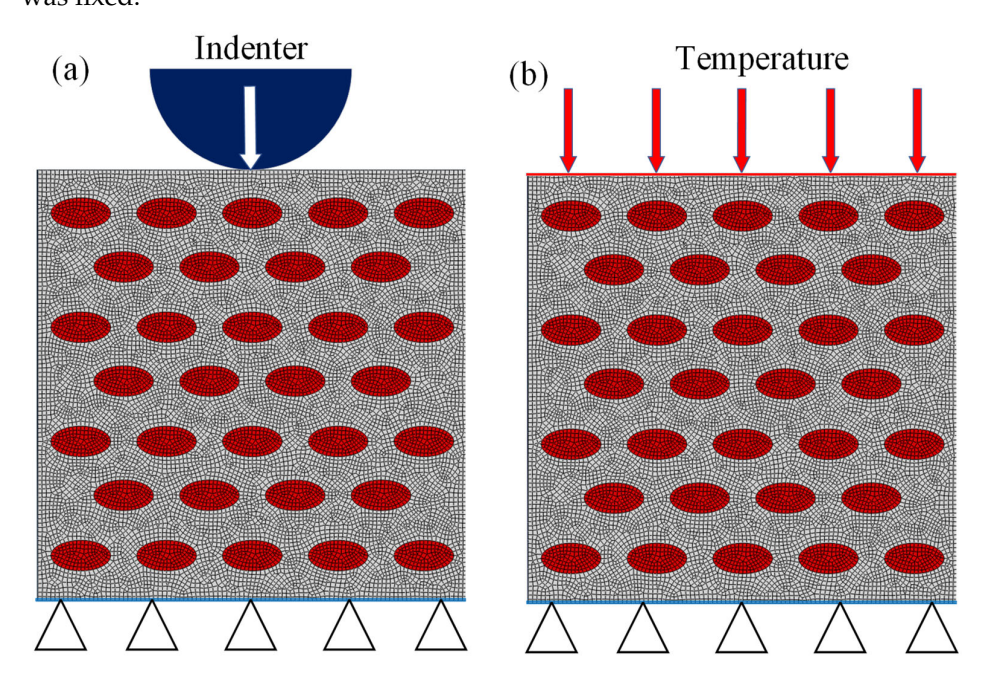


Figure 4. Finite element simulation calculation models. (a) EMAP TBCs compressive stress model; (b) EMAP TBCs thermal stress model.

## 2.3. Orthogonal Experimental Design

An orthogonal experimental design is a method to study multifactorial multilevel experiments. In this paper, orthogonal experiments were used to establish a sample set for machine learning and were combined with the method of analysis of extreme variance to analyze the extent of the effect of microstructural characteristics of EMAP TBCs on their strain tolerance and thermal insulation performance. Ovality, horizontal angle, vertical distance, density, and top distance of the MAP are used as the design variables. As shown in Table 2, four equidistant levels were used for each of the five factors of the microstructural characterization.

Level	Ovality	Horizontal Angle (°)	Vertical Distance (µm)	Density	Top Distance (μm)
1	0.5	20	21	0.22	12
2	0.6	30	22	0.24	14
3	0.7	40	23	0.26	16

24

Table 2. Factor level table.

50

4

0.8

After determining the data and levels of each factor, the orthogonal test program was determined based on the selected 5-factor, 4-level table. The orthogonal design table is shown in Table 3, where the L16 (45) orthogonal test table is selected, and the values in the table are the data of different levels of the corresponding factors. According to the orthogonal design table, it can be seen that the test data are divided into 16 groups by cross-combination, and the different test numbers represent a group of data. The data

0.28

18

Coatings **2025**, 15, 24 7 of 19

in the corresponding factor level table are substituted into the finite element simulation calculation model to calculate the EMAP TBCs compressive stress and thermal stresses of the different combinations of data. The compressive stress, thermal stress data, and each factor calculated by the finite element method were substituted into the numerical model of the range analysis for calculation. The calculated range value (R-value) was used to determine the influence of different microstructure characteristic factors on compressive stress and thermal stress.

Serial Number	Ovality	Horizontal Angle (°)	Vertical Distance (µm)	Density	Top Distance (μm)
1	1	1	1	1	1
2	1	2	2	2	2
3	1	3	3	3	3
4	1	4	4	4	4
5	2	1	2	3	4
6	2	2	1	4	3
7	2	3	4	1	2
8	2	4	3	2	1
9	3	1	3	4	2
10	3	2	4	3	1
11	3	3	1	2	4
12	3	4	2	1	3
13	4	1	4	2	3
14	4	2	3	1	4
15	4	3	2	4	1
16	4	4	1	3	2

# 2.4. Machine Learning Modeling

In this paper, a machine learning model is established, in which the input is microstructure data and the output is coating performance data. The microstructure data include the density, horizontal angle, ovality, vertical distance, and top distance of MAP. The coating performance data include coating compressive stress and thermal stress data. The input and output data are used to establish a data set to train the machine learning model. To confirm the accuracy of the prediction results, as well as to compare the prediction performance of the prediction models, this paper used the traditional back propagation (BP) neural network model, support vector machine (SVM) regression prediction model, and particle swarm optimization algorithm-support vector machine (PSO-SVM) regression prediction model three prediction models for EMAP TBCs.

### 2.4.1. BP Neural Network Regression Prediction Model

A BP neural network is a multi-layer feedforward neural network based on an error backpropagation algorithm that trains the network by establishing a set of error functions to minimize the error between the desired outputs [26,27].

Specifically, BP neural network prediction can be divided into the following steps:

- (1) Forward propagation: pass the input data through the input layer to the hidden layer and the output layer and calculate the output result.
- (2) Error calculation: the error between the calculated output result and the actual target value is passed back to the network, and the error value is calculated.
- (3) Backpropagation: calculate the gradient of each neuron, i.e., the partial derivatives of the weights and biases to the error, layer-by-layer from the output layer to the input layer according to the error value and the chain rule.

Coatings 2025, 15, 24 8 of 19

(4) Updating the weights and biases: adjusting the weights and biases of each neuron according to the calculated gradient information to reduce the error value and improve the accuracy of the neural network.

# 2.4.2. Support Vector Machine (SVM) Regression Prediction Model

SVM is a machine learning algorithm based on supervised learning. The SVM regression prediction algorithm is different from the traditional regression prediction algorithm, and its goal is to find an optimal hyperplane of the data in a high-dimensional feature space. The regression prediction task is realized by constructing a prediction function to minimize the difference between the predicted result and the actual result, and considering the maximum interval between the support vector and hyperplane [28].

The SVM prediction steps are as follows:

(1) Linear SVM Regression Model: Find a linear function to best fit the data. The form of this linear function is usually expressed as

$$f(x) = w^t + b \tag{1}$$

where f(x) is the predicted output, w is the weight vector, x is the input feature vector, b is the bias.

(2) Optimization objective function of SVM regression: the objective of SVM regression is to minimize the prediction error and maintain the interval. Here the slack variable  $\varepsilon$  is introduced to allow the error of some data points, while the minimization error and maximization interval are balanced by the parameter C. The optimization objective formula is as follows:

$$\min_{w,b,\varepsilon} = \frac{1}{2} \|w\|^2 + C \sum_{i=1}^{m} \left(\varepsilon_{i+\varepsilon_i^*}\right)$$
 (2)

where  $\|w\|^2$  is a regular term, C is a regularization parameter,  $\varepsilon_i$  and  $\varepsilon_i^*$  is a relaxation variable.

(3) Constraints: constraints for SVM regression are used to ensure that the prediction error is limited to a certain range:

$$y_i - \langle w, x_i \rangle - b \le \varepsilon + \varepsilon_i \tag{3}$$

$$\varepsilon_i, \varepsilon_i^* > 0$$
 (4)

where  $x_i$  is the input eigenvector of the *i*th sample in the training set, and  $y_i$  is the corresponding output value.

### 2.4.3. Particle Swarm Optimization (PSO) Algorithm

PSO algorithm is a stochastic search algorithm based on group collaboration developed by simulating the foraging behavior of a flock of birds. The PSO optimization algorithm is simple and easy to implement, has a strong global search capability, and is able to find the global optimal solution [29]. The particle velocity and position update formulas are as follows:

Speed Updates:

$$v[i] = w \times v[i] + c_1 \times r_{and} \times (pbest[i] - x[i]) + c_2 \times r_{and} \times (gbest - x[i])$$
 (5)

**Location Updates:** 

$$x[i] = x[i] + v[i] \tag{6}$$

Coatings 2025, 15, 24 9 of 19

where: v[i] is the velocity of the first particle, w s the inertia weight,  $c_1$  and  $c_2$  is the learning factor,  $r_{and}$  is a random number from 0 to 1, and pbest[i] is the optimal value searched by the ith particle, gbest is the optimal value searched by the whole cluster.

As shown in Figure 5, a flowchart of the PSO algorithm implementation is shown, which specifically includes the following steps:

- Step 1: Generate a set of particles randomly and initialize the position and velocity of the particles;
- Step 2: Solve the fitness value of each particle using the fitness function, and update the position and velocity of the particle.
- Step 3: Calculate the fitness of the particle again; if the calculated fitness of the particle is the optimal fitness, then update its pbest, and update the gbest at the same time;
- Step 4: Set the maximum number of iterations of the optimization algorithm to 120, and repeat the calculation of the above steps until the termination condition is satisfied and the calculation is finished.

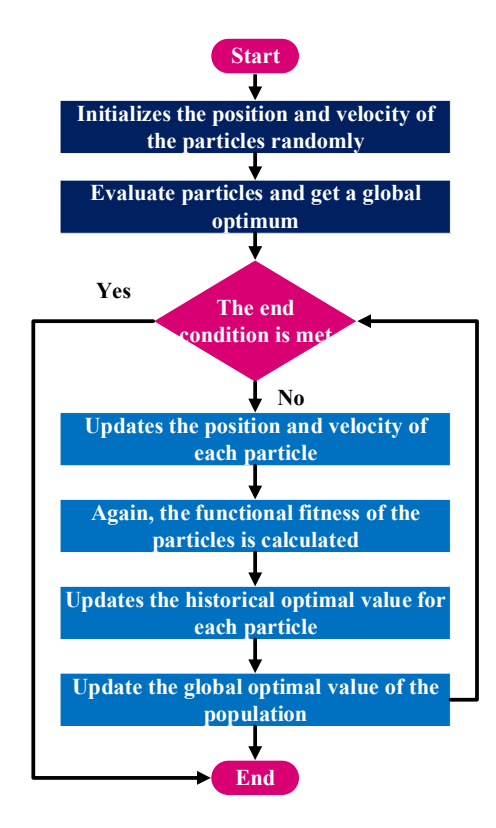


Figure 5. Flowchart of PSO algorithm optimization.

### 2.4.4. SVM Regression Prediction Model Optimized by PSO Algorithm

The SVM regression prediction algorithm is an application of a support vector machine to the regression prediction problem. In general, in an SVM regression algorithm, some of its key parameters, such as the penalty coefficient parameter  $\varepsilon$ , insensitivity coefficient parameter  $\varepsilon$ , and kernel function parameter  $\gamma$ , usually need to be set according to the engineer's experience, which has certain uncertainty and blindness. Therefore, in this paper, we use the PSO optimization algorithm to optimize the three parameters ( $\varepsilon$ ,  $\varepsilon$ ,  $\gamma$ ) of the SVM regression algorithm to form a better machine learning model [30].

To further analyze the prediction performance and prediction accuracy of the three machine learning models, BP neural network, SVM, and PSO-SVM, the coefficient of

Coatings **2025**, 15, 24 10 of 19

determination R2, Root Mean Square Error (RMSE), and Mean Absolute Error (MAE) were used as the model evaluation metrics [31], and the computational equation is as follows:

$$R^{2} = 1 - \sqrt{\frac{\sum_{i=1}^{n} (y - y'^{2})}{\sum_{i=1}^{n} y'^{2}}}$$
 (7)

$$RMSE = \sqrt{\frac{\sum_{i=1}^{n} (y - y')^2}{n}}$$
 (8)

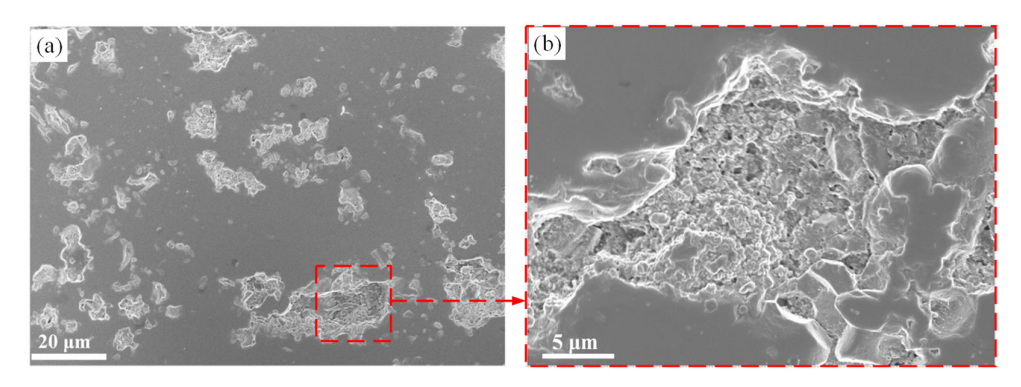
$$MAE = \frac{\sum_{i=1}^{n} |y - y'|}{n}$$
(9)

where y is the true value, y' is the predicted value, and n is the number of samples.

### 3. Results and Discussion

### 3.1. Microstructure Characterization of EMAP TBCs

By improving the plasma powder feeding process, the second phase MAP was successfully introduced to change the microstructure of TBCs. As shown in Figure 6, the cross-section SEM image of the EMAP TBC ceramic layer was prepared by a special powder feeding process. Figure 6a shows the local cross-section. It can be clearly seen that MAP is irregularly embedded in the dense conventional coating after the plasma beam impact. Figure 6b shows a local enlargement of the cross-section of the ceramic layer. It can be clearly seen that the internal structure of the MAP still maintains the porous microstructure after plasma spraying.



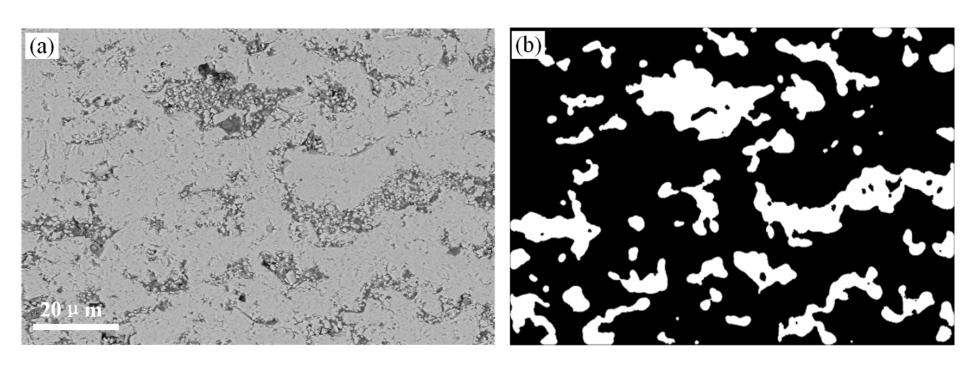
**Figure 6.** SEM image of the cross-section of the ceramic layer of the EMAP TBCs. (a)  $1000 \times$  cross-section SEM image; (b)  $3500 \times$  SEM image.

Figure 7 shows the MAP regions that were extracted and characterized using a machine learning approach, where the white areas are the MAP distribution regions. The characterization results were measured using ImageJ (Version 1.54a) to obtain the MAP density, which ranged from 19.5% to 29.1%. The TBC microstructure has an important effect on its service performance; therefore, it is of great significance to study the microstructural characteristics of EMAP TBCs.

Figure 8 shows the microstructure characterization diagram of the EMAP TBC. The most important structural feature of EMAP TBCs is the conventional coating obtained at a higher power, in which porous MAP particles are embedded. Therefore, the distribution morphology and density of MAP are the main microstructure characteristics of the coating. By measuring the total thickness of the coating and the number of spray gun movements, the thickness of a single plasma spraying is calculated to be about 20  $\mu m$ . As conventional coatings were deposited, the MAPs were embedded in a layered structure in the form of waves stacked on top of each other. After observing and analyzing the SEM image of

Coatings 2025, 15, 24 11 of 19

the coating, it can be seen that the MAP is diffusely distributed inside the coating in an ellipse-like morphology; thus, the MAP was equated to an ideal ellipse during the analysis process. The distribution morphology of the MAP was expressed using the horizontal angle, ovality, vertical distance, and horizontal distance of the equivalent posterior ellipse. As shown in Figure 8a, it can be observed that the MAP was embedded into the coating of the layer structure in the form of different ovalities and different horizontal angles, and the vertical distance is the distance of each layer of MAP in the direction perpendicular to the horizontal. As shown in Figure 8b, the top distance is the distance of the center of the first MAP layer from the top distance of the coatings.



**Figure 7.** EMAP TBCs micro-aggregate particle feature extraction (**a**) EMAP TBCs microstructure (**b**) EMAP TBCs microstructure extraction.

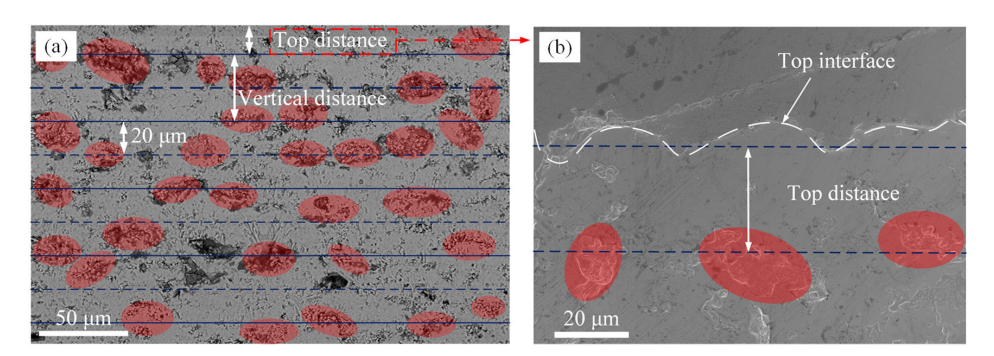


**Figure 8.** EMAP TBCs microstructure characterization plots. (a) Overall microstructure characterization plot; (b) Top distance characterization plot.

Figure 9 shows how to define the ellipticity and angle of MAP particles; an ellipse's ovality is the ratio of the short axis b to the long axis a. The horizontal angle of the ellipse is the angle between the long axis of the ellipse and the positive half-axis in the horizontal direction.

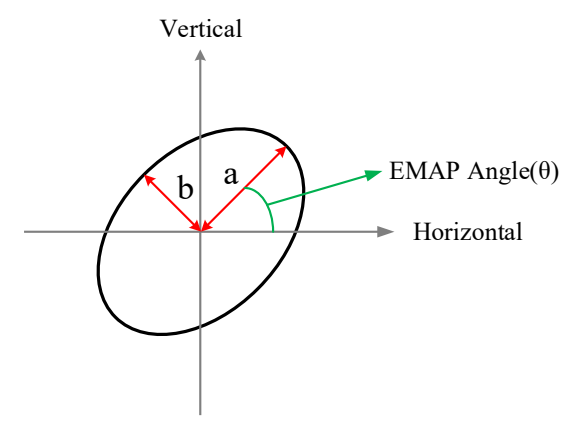
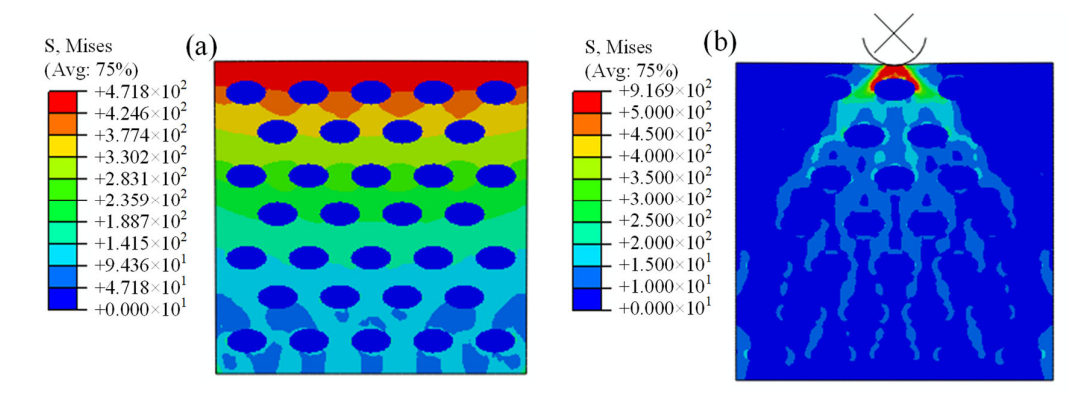


Figure 9. MAP structure analysis diagram.

Coatings 2025, 15, 24 12 of 19

### 3.2. Finite Element Analysis

Figure 10 shows the Mises stress distribution cloud of the EMAP TBCs inside the coating under indenter load and temperature load, respectively. The added EMAP was able to significantly relieve the EMAP TBC stress near the front of the indentation, and due to its internal loose and porous structure, has an obvious effect on the alleviation of the thermal stresses, this results in improved strain tolerance and thermal insulation performance of the coating. The addition of MAP has a significant effect on the performance of TBCs; therefore, the main microstructural features of EMAP TBCs are the distribution morphology and density of MAP, and it is important to investigate the effects of different distribution morphologies and densities of MAP on the strain tolerance and thermal insulation performance of coatings to further improve the thermal insulation performance of sintering resistance of TBCs.



**Figure 10.** Finite element calculation result plots. (a) EMAP TBCs thermal stress calculation cloud; (b) EMAP TBCs compressive stress calculation cloud.

Figure 11 shows the influence of the changed microstructure characteristics of the EMAP TBC on its strain tolerance. As shown in Figure 11a, the effect of the horizontal angle change of MAP on the coating strain tolerance was analyzed by studying the effect of the horizontal angle change of MAP on the compressive stress. It can be observed from the dotted line graph that the coating compressive stress appears to increase and then decrease as the horizontal angle increases. In the horizontal angle range of 0–90°, the coating compressive stress increased from 891.1 Pa to 1011 Pa and then decreased from 1011 Pa to 901.6 Pa in the  $90-170^{\circ}$  range. With the change in the horizontal angle in the range of 0–170°, the corresponding compressive stress does not change symmetrically. This is because although the ellipses on both sides of 90° are symmetrically distributed, the distribution structure is still different, resulting in different compressive stress results. As shown in Figure 11b, with the change of MAP density and ovality, and the corresponding coating compressive stress results are shown in the graph. From the dotted line graph, it can be intuitively seen that as the MAP density increases within a certain range, the maximum average compressive stress of the coating gradually decreases, from the initial 1143 Pa to 823.5 Pa; this indicates that with the increase in MAP density, the ability of the coating to alleviate stress concentration increases, and its strain tolerance performance is significantly improved. In addition, with the increase in MAP ellipticity, the compressive stress of the coating shows a significant upward trend, indicating that the increase in ellipticity is not conducive to improving the strain tolerance performance of the coating. After the analysis, when the horizontal angle of the MAP is  $0^{\circ}$ , the maximum average stress is minimized, and its strain tolerance performance is optimal. The top distance of the MAP coating is another important microstructural feature, as shown in Figure 11c, and it is seen from the dotted line graph that the compressive stress of the coating rises gradually with the increase in the top distance. The top distance is within the range of 8–48 μm, and the

Coatings 2025, 15, 24 13 of 19

compressive stress of the coating increased from 666.9 Pa to 1286 Pa. In addition, the effect of the vertical distance between each layer of MAP on the strain tolerance of the coating was also explored in the vertical direction perpendicular to the bottom of the coating. As shown in Figure 11d, the clear reflection of the dotted line graph shows that as the vertical distance increases within the range of 18–35  $\mu$ m, the compressive stress of the coating has an upward trend. Therefore, the vertical distance and top distance have a similar impact on the strain tolerance of the coating; that is, their strain tolerance performance decreases with the increase in distance values.

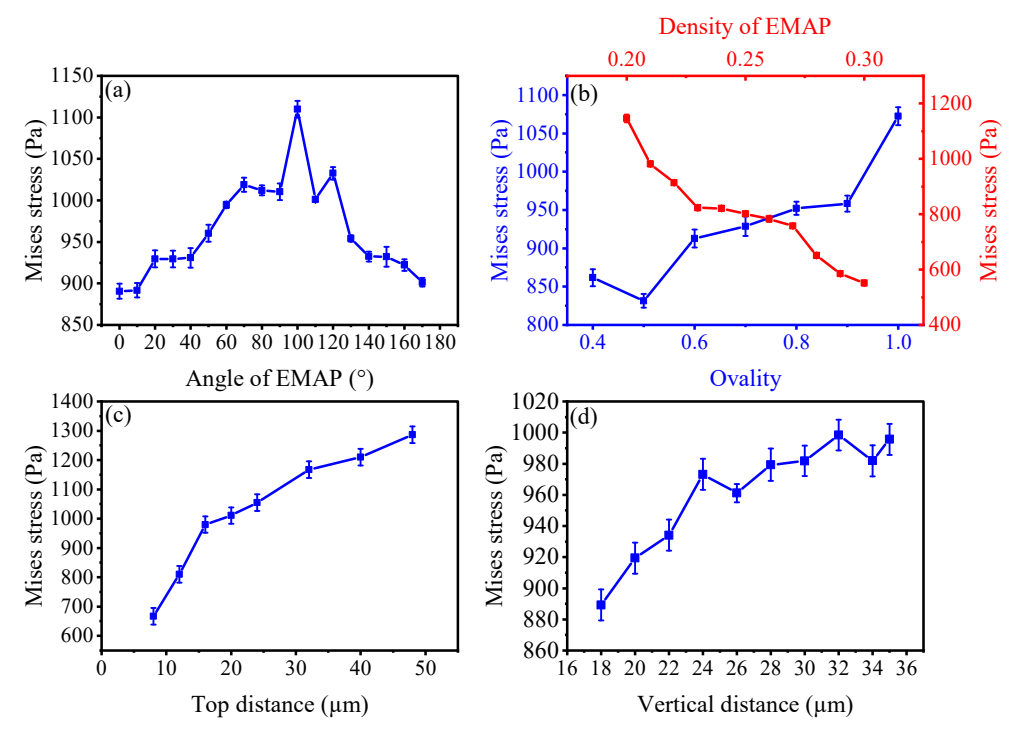


**Figure 11.** Effect of microstructure characteristics on compressive stress of coating. (a) Effect of MAP horizontal angle on compressive stress; (b) The influence of MAP density and ovality on compressive stress; (c) Effect of MAP apex distance on compressive stress; (d) Effect of MAP vertical distance on compressive stress.

Figure 12 shows the effect of changing the microstructure characteristics of the EMAP TBC on its thermal insulation performance. Thermal insulation performance is another important aspect of EMAP TBCs. Due to the fact that the thermal load added to the top of all simulation models (near the heat flow end) is 1100 °C, the simulation results show that the thermal stress at the top of the coating simulation model with the same feature remains at the same value. Therefore, in the statistical process, only the maximum average thermal stress change at the bottom position of the coating simulation model was analyzed to evaluate the thermal insulation performance of the EMAP TBCs. As shown in Figure 12a, when the horizontal angle is within the range of 0-90°, the thermal stress of the coating increases from the initial 201.1 Pa to 316.4 Pa and then decreases from 316.4 Pa to 210.9 Pa within the range of 90–170°. Therefore, when the MAP horizontal angle is 0°, the thermal stress of the coating is minimized, indicating that the insulation performance of the coating is optimal. When the horizontal angle is 90°, the thermal stress of the coating is the highest, indicating that the insulation performance of the coating is the worst. As shown in Figure 12b, the thermal stress of the coating exhibits a certain degree of fluctuation with the change in the MAP vertical distance. Within the range of 18–22 μm, the thermal stress sharply decreases, and after 22 µm, the decrease slows down until reaching the minimum value at 28 μm. Then, in the range of 28–34 μm, the thermal stress shows an Coatings 2025, 15, 24 14 of 19

upward trend. The analysis results indicate that the thermal insulation performance of the coating reaches its optimal level at a vertical distance of  $28~\mu m$ . As the distance from the top changes, the thermal stress of the coating decreases within the range of 8– $16~\mu m$  and gradually increases within the range of 16– $48~\mu m$ . Therefore, at  $16~\mu m$ , the thermal stress of the coating reaches its minimum value, and its thermal insulation performance is optimal. As shown in Figure 12c, the thermal stress results corresponding to the variation in MAP ellipticity are presented. From the dotted line graph, it can be intuitively seen that as the ellipticity increases, the thermal stress of the coating gradually increases, and the thermal insulation performance of the coating decreases. As shown in Figure 12d, the results of changing the MAP density and coating thermal stress are presented. From the line graph, it can be clearly seen that as the MAP density increases, the thermal stress values gradually decrease within the range of 0.20–0.27. Within the range of 0.27–0.30, as the proportion density increases, the thermal stress values tend to stabilize, indicating that the thermal insulation performance of the coating improves within a certain range with the increase in MAP density.

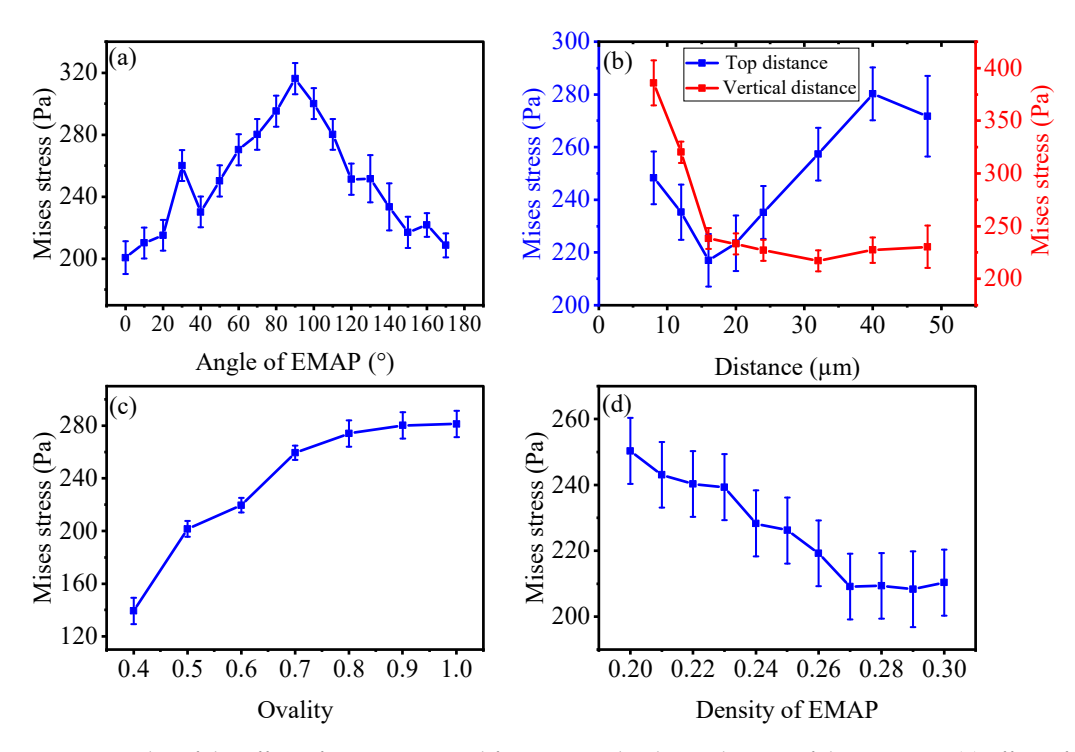


**Figure 12.** Plot of the effect of microstructural features on the thermal stress of the coatings. (a) effect of MAP horizontal angle on thermal stress; (b) effect of MAP top distance and vertical distance on thermal stress; (c) effect of MAP ovality on thermal stress; and (d) effect of MAP density on thermal stress.

The results show a certain regularity in the effect of EMAP TBCs' microstructural characteristics on their strain tolerance and thermal insulation performance. As the MAP density increases in the range of 0.2–0.3, the strain tolerance and thermal insulation performance of the coatings are enhanced. As the MAP ovality increases in the range of 0.4–1, both the strain tolerance and thermal insulation performance of the coatings decrease. As the horizontal angle of the MAP increases in the range of 0–170°, the strain tolerance and thermal insulation performance of the coatings show a decreasing and then an increasing trend. The strain tolerance and thermal insulation performance of the coatings were different for the top distance and vertical distance of the MAP, with both values showing a decreasing trend in the strain tolerance and an increasing and then decreasing trend in the thermal insulation performance. The thermal insulation performance was optimal at 28  $\mu m$  for a vertical distance of 16  $\mu m$  and a top distance.

Coatings 2025, 15, 24 15 of 19

# 3.3. Orthogonal Experimental Design Analysis Results

Table 4 shows the orthogonal experimental design; experimental data with different microstructural features were combined to calculate the compressive and thermal stresses of the EMAP TBCs finite element model. The calculation results of the finite element simulation tests corresponding to different combinations are different. The calculated results were substituted into the range analysis model and analyzed using IBM SPSS (Version 25.0.0.2) software. The analysis results are shown in Tables 4 and 5, in which the K-value is the sum of the experimental data at a certain level of a factor, the K<sub>avg</sub> value is the corresponding average value, and R is the range value of the factors. The R-value is used to reflect the influence of the change in the factors on the analytical performance. The larger the R-value, the greater the influence of the factors on the coating performance.

<b>Table 4.</b> Finite element s	imulation test ca	alculation results.
----------------------------------	-------------------	---------------------

Serial Number	Ovality	Horizontal Angle (°)	Vertical Distance (µm)	Density	Top Distance (µm)	Compressive Stress (Pa)	Thermal Stress (Pa)
1	1	1	1	1	1	828.5	239.314
2	1	2	2	2	2	861.2	251.998
3	1	3	3	3	3	750	279.094
4	1	4	4	4	4	775.3	282.101
5	2	1	2	3	4	773.2	252.746
6	2	2	1	4	3	747.6	245.02
7	2	3	4	1	2	967.9	297.313
8	2	4	3	2	1	1093	302.291
9	3	1	3	4	2	785.8	264.405
10	3	2	4	3	1	869.6	289.417
11	3	3	1	2	4	724.4	304.76
12	3	4	2	1	3	824.1	321.995
13	4	1	4	2	3	849.9	298.33
14	4	2	3	1	4	844.1	310.32
15	4	3	2	4	1	786.4	286.984
16	4	4	1	3	2	1141	307.718

**Table 5.** Range analysis table of the influencing factors of compressive stress.

Term	Level	Ovality	Horizontal Angle (°)	Vertical Distance (µm)	Density	Top Distance (μm)
	1	3215.00	3237.40	3441.50	3464.60	3577.50
1/ 1	2	3581.70	3322.50	3244.90	3528.50	3755.90
K-value	3	3203.90	3228.70	3472.90	3533.80	3171.60
	4	3621.40	3833.40	3462.70	3095.10	3117.00
	1	803.75	809.35	860.38	866.15	894.38
1/ 1	2	895.43	830.63	811.23	882.13	938.97
K-value	3	800.98	807.18	868.23	883.45	792.90
	4	905.35	958.35	865.67	773.77	779.25
F	<u> </u>	104.38	151.17	57.00	109.68	149.72
Number	of levels	4	4	4	4	4
Number of repli	cates per level r	4.0	4.0	4.0	4.0	4.0

As shown in Table 5, it is the result of the range analysis of the influencing factors of compressive stress. According to the comparison of the R-value of each factor, the primary factor affecting the compressive stress is the horizontal angle, followed by the density, horizontal angle, ovality, and vertical distance. Therefore, the primary and secondary order of the influencing factors in the strain tolerance performance of EMAP TBCs was horizontal angle > top distance > density > ovality > vertical distance.

Coatings **2025**, 15, 24 16 of 19

As shown in Table 6 below, it is the result of the range analysis of the influencing factors of the thermal stress. According to the R-value of each factor, the primary factor affecting the thermal stress is the horizontal angle, followed by the ovality, density, vertical distance, and top distance. Therefore, the primary and secondary factors affecting the thermal insulation performance of EMAP TBCs were horizontal angle > ovality > density > vertical distance > top distance.

Term	Level	Ovality	Horizontal Angle (°)	Vertical Distance (μm)	Density	Top Distance (μm)
	1	1052.51	1054.79	1096.81	1168.94	1118.01
7/ 1	2	1097.37	1096.75	1113.72	1157.38	1121.43
K-value	3	1180.58	1168.15	1156.11	1128.98	1144.44
	4	1203.35	1214.11	1167.16	1078.51	1149.93
	1	263.13	263.70	274.20	292.24	279.50
77. 1	2	274.34	274.19	278.43	289.34	280.36
K-value	3	295.14	292.04	289.03	282.24	286.11
	4	300.84	303.53	291.79	269.63	287.48
R	}	37.71	39.83	17.59	22.61	7.98
Number	of levels	4	4	4	4	4
Jumber of repli	cates per level r	4.0	4.0	4.0	4.0	4.0

Table 6. Range analysis table of influencing factors of thermal stress.

In a comprehensive analysis, based on the degree of influence of different microstructural characterization factors on the strain tolerance and thermal insulation performance of EMAP TBCs, the obvious factor that had the most significant effect on the sintering resistance of EMAP TBCs was the horizontal angle of MAP, followed by ovality and density.

### 3.4. Machine Learning

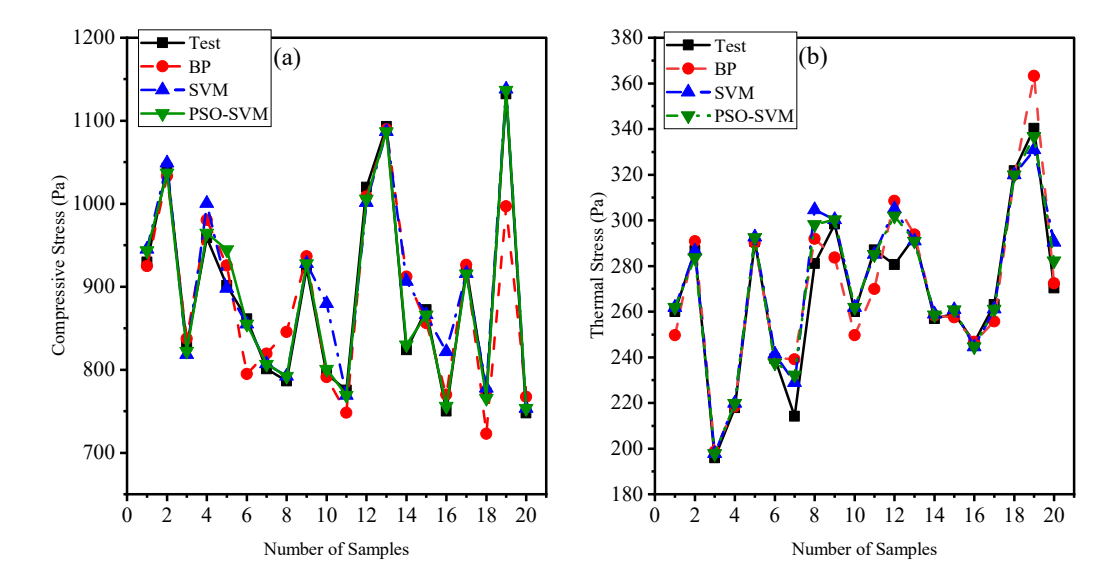
Based on the above finite element model calculation data, a machine learning model was established. A total of 100 sets of EMAP TBCs microscopic feature data, corresponding to 100 groups of coating compressive stress and thermal stress data, and the datasets corresponding to compressive stress and thermal stress were constructed, and 80% of the dataset was used for training and 20% for prediction. Using the data of MAP density, horizontal angle, ovality, vertical distance, and tip distance as inputs and the corresponding compressive stress and thermal stress as outputs, the accuracy of predicting the strain tolerance and thermal insulation performance of EMAP TBC microstructure features as inputs was explored, which was helpful for further improving the strain tolerance and thermal insulation performance of TBCs. In this study, three machine learning models, namely, the BP neural network model, the SVM regression prediction model, and the PSO-SVM regression prediction model, were used to predict the performance of EMAP TBCs to explore the prediction performance and accuracy of different machine learning prediction models.

Figure 13a,b shows the prediction results of the three machine learning prediction models for the compressive stress and thermal stress of the coating, respectively. Through observation, it can be clearly seen that the machine learning method is more accurate in predicting the performance of EMAP TBCs. By comparing the fitting degree of the three machine learning prediction models, it can be found that the PSO-SVM regression prediction model has the highest fitting degree and the best prediction effect among the three fitting results.

As shown in Table 7, the RMSE and MAE of the BP neural network model were 44.78 and 30.32, respectively, and the RMSE and MAE of the SVM model were 33.13 and 20.00. Respectively, the RMSE and MAE of the PSO-SVM model were only 11.93 and 8.56. The regression coefficients  $R^2$  of BP and SVM were 0.841 and 0.913, respectively, while

Coatings 2025, 15, 24 17 of 19

the  $R^2$  of PSO-SVM was the most excellent at 0.988. Similarly, as shown in Table 8, for the thermal stress prediction of coatings, the error of the PSO-SVM prediction model is the smallest, and the  $R^2$  was the best at 0.945.



**Figure 13.** Machine learning prediction results. (a) compressive stress prediction results; (b) prediction results of thermal stress.

**Table 7.** Analysis of compressive stress prediction error.

Predictive Models	R <sup>2</sup>	RMSE	MAE
BP	0.841	44.78	30.32
SVM	0.913	33.13	20.00
PSO-SVM	0.988	11.93	8.56

Table 8. Analysis of thermal stress prediction error.

Predictive Models	$\mathbb{R}^2$	RMSE	MAE
BP	0.878	11.95	8.12
SVM	0.918	9.78	5.97
PSO-SVM	0.945	8.06	5.09

The results show that the machine learning model is established to predict the strain tolerance and thermal insulation performance of the coating to achieve the purpose of evaluating the anti-sintering performance of the coating, and the results show a certain prediction accuracy. The PSO-SVM prediction model was used to evaluate the strain tolerance and thermal insulation performance of the coating, and the prediction effect was the best. Combined with the error index and the regression coefficient R<sup>2</sup> to evaluate the performance of different prediction models, the results show that the error indexes of the PSO-SVM prediction model are lower than those of the BP neural network model and the SVM prediction model, and the R<sup>2</sup> is the highest. This indicates that the PSO-SVM prediction model is the best in the evaluation of the strain tolerance and thermal insulation performance parameters of the coating and has higher accuracy and reliability.

# 4. Conclusions

In this study, a data-mechanism hybrid model based on experimental research, simulation, calculation, and machine learning was established to analyze the influence of coating microstructure characteristics on its sintering resistance. Key findings include:

Coatings 2025, 15, 24 18 of 19

(1) EMAP TBCs are mainly composed of dense coating substrates and porous micron particles. The microstructure characteristics of the prepared EMAP TBCs were analyzed and simulated for calculation. The results show that the main microstructure characteristics of EMAP TBCs affect its sintering resistance, and the strain tolerance and thermal insulation performance of the coating can be optimized by adjusting the microstructure characteristic data of EMAP TBCs to optimize its sintering resistance.

- (2) The influence of the EMAP TBC microstructure characteristic factors on the antisintering performance of the coating was comprehensively analyzed. The most obvious factors that have the most significant impact on the sintering resistance of EMAP TBCs were the horizontal angle of MAP, followed by ovality and density.
- (3) Ae machine learning model was applied to evaluate the nonlinear relationship between the microstructure characteristic data of EMAP TBCs and their anti-sintering performance. The results show that the machine learning model can be prepared for evaluation, and PSO-SVM has the highest prediction accuracy and the best prediction effect, making it the best model for evaluating the anti-sintering performance of EMAP TBCs.

In this study, the effect of the microstructure of EMAP TBCs on sintering resistance was systematically analyzed, and a reference for further improving the sintering resistance of TBCs was provided. In the future, the microstructure can be further optimized by changing the spraying process parameters, such as the powder feeding rate, before the engineering application in order to obtain a coating with better performance.

**Author Contributions:** Conceptualization, D.Y., S.X., Z.X., C.Y., Y.W. and H.L.; Data curation, S.X.; Funding acquisition, D.Y.; Investigation, D.Y., S.X. and T.Y.; Methodology, S.X., J.P., C.Y., Y.W. and H.L.; Project administration, D.Y., Z.X., J.P., H.L., T.Y. and J.H.; Resources, Z.X., J.P. and J.H.; Software, D.Y., S.X., C.Y. and T.Y.; Supervision, D.Y., Z.X., T.Y. and J.H.; Validation, D.Y. and S.X.; Writing—original draft, D.Y. and S.X.; Writing—review and editing, D.Y., S.X., Z.X. and J.H. All authors have read and agreed to the published version of the manuscript.

**Funding:** This research was funded by the National Natural Science Foundation of China (No. 52205547, D.Y.), the Excellent Young Talents Fund of Higher Education Institutions of Anhui Province (No. 2024AH030006, D.Y.), the Key Research and Development Projects in Anhui Province (2022a05020004, D.Y.), Industry–University Research Project (No. HX-2024-04-054, D.Y., No. HX-2024-09-085, D.Y.), the Undergraduate Teaching Quality Improvement Program Project of Anhui Polytechnic University (No. 2023jyxm76, D.Y., No. 2023szyzk39, D.Y., 2024szyzk51).

Institutional Review Board Statement: Not applicable.

Informed Consent Statement: Not applicable.

**Data Availability Statement:** Data are contained within the article.

Conflicts of Interest: The authors declare no conflicts of interest.

### References

- 1. Wei, Z.Y.; Meng, G.H.; Chen, L.; Li, G.R.; Liu, M.J.; Zhang, W.X.; Zhao, L.N.; Zhang, Q.; Zhang, X.D.; Wan, C.L. Progress in ceramic materials and structure design toward advanced thermal barrier coatings. *J. Adv. Ceram.* 2022, 11, 985–1068. [CrossRef]
- 2. Lee, D.H.; Lee, K.S.; Kim, T.W.; Kim, C. Hertzian stress analysis and characterization of thermal barrier coatings containing unidirectional vertical cracks. *Ceram. Int.* **2019**, *45*, 21348–21358. [CrossRef]
- 3. Ganvir, A.; Curry, N.; Markocsan, N.; Nylén, P.; Toma, F.-L. Comparative study of suspension plasma sprayed and suspension high velocity oxy-fuel sprayed YSZ thermal barrier coatings. *Surf. Coa. Technol.* **2015**, 268, 70–76. [CrossRef]
- 4. Gupta, M.; Dwivedi, G.; Nylén, P.; Vackel, A.; Sampath, S. An Experimental Study of Microstructure-Property Relationships in Thermal Barrier Coatings. *J. Therm.l Spray Technol.* **2013**, 22, 659–670. [CrossRef]
- 5. Li, F.; Xie, Y.; Yang, L.; Zhou, Y.; Zhu, W. Study on cyclic thermal corrosion behavior of APS-7YSZ thermal barrier coating at roomand high temperature. *Ceram. Int.* **2021**, *47*, 29490–29498. [CrossRef]

Coatings 2025, 15, 24 19 of 19

6. Lin, M.; Zhuo, J.; Huang, S.; Zhang, Q.; Zhang, Q.M. Sandwich-structured polymer dielectrics exhibiting significantly improved capacitive performance at high temperatures by roll-to-roll physical vapor deposition. *Chem. Eng. J.* **2024**, 498, 155586. [CrossRef]

- 7. Rüßmann, M.; Bakan, E.; Schrüfer, S.; Guillon, O.; Vaßen, R. Investigation of the cooling hole blockage induced by different thermal spray TBC deposition processes. *Surf. Coat. Technol.* **2024**, 493, 131278. [CrossRef]
- 8. Zhang, W.W.; Wei, Z.Y.; Zhang, L.Y.; Xing, Y.Z.; Zhang, Q. Low-thermal-conductivity thermal barrier coatings with a multi-scale pore design and sintering resistance following thermal exposure. *Rare. Met.* **2020**, *39*, 352–367. [CrossRef]
- 9. Padture, N.P. Advanced structural ceramics in aerospace propulsion. Nat. Mater. 2016, 15, 804–809. [CrossRef]
- 10. Ghasemi, R.; Vakilifard, H. Plasma-sprayed nanostructured YSZ thermal barrier coatings: Thermal insulation capability and adhesion strength. *Ceram. Int.* **2017**, *43*, 8556–8563. [CrossRef]
- 11. Lv, B.; Mücke, R.; Fan, X.; Wang, T.J.; Guillon, O.; Vaßen, R. Sintering resistance of advanced plasma-sprayed thermal barrier coatings with strain-tolerant microstructures. *J. Eur. Ceram. Soc.* **2018**, *38*, 5092–5100. [CrossRef]
- 12. Huang, J.B.; Wang, W.Z.; Li, Y.J.; Fang, H.J.; Ye, D.D.; Zhang, X.C.; Tu, S.T. Novel-structured plasma-sprayed thermal barrier coatings with low thermal conductivity, high sintering resistance and high durability. *Ceram. Int.* **2021**, 47, 5156–5167. [CrossRef]
- 13. Vagge, S.T.; Ghogare, S. Thermal barrier coatings: Review. Mater. Today Proc. 2022, 56, 1201–1216. [CrossRef]
- 14. McPherson, R. A review of microstructure and properties of plasma sprayed ceramic coatings. *Surf. Coat. Technol.* **1989**, *39*, 173–181. [CrossRef]
- 15. Mahade, S.; Jahagirdar, A.; Li, X.H.; Kjellman, B.; Björklund, S.; Markocsan, N. Tailoring microstructure of double-layered thermal barrier coatings deposited by suspension plasma spray for enhanced durability. *Surf. Coat. Technol.* **2021**, 425, 127704. [CrossRef]
- 16. Li, G.; Yang, G. Understanding of degradation-resistant behavior of nanostructured thermal barrier coatings with bimodal structure. *J. Mater. Sci. Technol.* **2019**, 35, 231–238. [CrossRef]
- 17. Lv, B.; Fan, X.; Li, D.; Wang, T.J. Towards enhanced sintering resistance: Air-plasma-sprayed thermal barrier coating system with porosity gradient. *J. Eur. Ceram. Soc.* **2018**, *38*, 1946–1956. [CrossRef]
- 18. Li, G.R.; Yang, G.J.; Li, C.X.; Li, C.J. Sintering characteristics of plasma-sprayed TBCs: Experimental analysis and an overall modelling. *Ceram. Int.* **2018**, *44*, 2982–2990. [CrossRef]
- 19. Huang, J.; Wang, W.; Li, Y.; Fang, H.; Ye, D.; Zhang, X.; Tu, S. Improve durability of plasma-splayed thermal barrier coatings by decreasing sintering-induced stiffening in ceramic coatings. *J. Eur. Ceram. Soc.* **2020**, *40*, 1433–1442. [CrossRef]
- 20. Cocks, A.; Fleck, N.; Lampenscherf, S. A brick model for asperity sintering and creep of APS TBCs. *J. Mech. Physi. Solids.* **2014**, 63, 412–431. [CrossRef]
- 21. Cipitria, A.; Golosnoy, I.O.; Clyne, T.W. Sintering Kinetics of Plasma-Sprayed Zirconia TBCs. *J. Therm. Spray Technol.* **2007**, 16, 809–815. [CrossRef]
- 22. Li, G.R.; Wang, L.S.; Yang, G.J. Achieving self-enhanced thermal barrier performance through a novel hybrid-layered coating design. *Mater. Des.* **2019**, *167*, 107647. [CrossRef]
- 23. Fartash, A.H.; Lyavoli, H.F.; Poursaeidi, E.; Schmauder, S. Interfacial delamination of porous thermal barrier coatings based on SEM image processing in finite element model. *Theor. Appl. Fract. Mech.* **2023**, *125*, 103915. [CrossRef]
- 24. Alkurdi, A.A.H.; Al-Mohair, H.K.; Rodrigues, P.; Alazzawi, M.; Sharma, M.K.; Oudah, A.Y. Enhancing Mechanical Behavior Assessment in Porous Thermal Barrier Coatings using a Machine Learning Fine-Tuned with Genetic Algorithm. *J. Therm. Spray Technol.* 2024, 33, 824–838. [CrossRef]
- 25. Li, R.; Ye, D.; Xu, Z.; Yin, C.; Xu, H.; Zhou, H.; Yi, J.; Chen, Y.; Pan, J. Nondestructive Evaluation of Thermal Barrier Coatings Thickness Using Terahertz Time-Domain Spectroscopy Combined with Hybrid Machine Learning Approaches. *Coatings* **2022**, *12*, 1875. [CrossRef]
- 26. Özel, S.; Vural, E.; Binici, M. Optimization of the effect of thermal barrier coating (TBC) on diesel engine performance by Taguchi method. *Fuel* **2020**, *263*, 116537. [CrossRef]
- 27. Rumelhart, D.E.; Hinton, G.E.; Williams, R.J. Learning representations by back-propagating errors. *Nature.* **1986**, 323, 533–536. [CrossRef]
- 28. Dudzik, W.; Nalepa, J.; Kawulok, M. Evolving data-adaptive support vector machines for binary classification. *Knowl. B. Syst.* **2021**, 227, 107221. [CrossRef]
- 29. Elloumi, W.; Baklouti, N.; Abraham, A.; Alimi, A.M. The multi-objective hybridization of particle swarm optimization and fuzzy ant colony optimization. *J. Intell. Fuzzy System* **2014**, 27, 515–525. [CrossRef]
- 30. Tan, X.; Yu, F.; Zhao, X. Support vector machine algorithm for artificial intelligence optimization. *Cluster Comput.* **2019**, 22, 15015–15021. [CrossRef]
- 31. Wang, W.; Lu, Y. Analysis of the Mean Absolute Error (MAE) and the Root Mean Square Error (RMSE) in Assessing Rounding Model. *IOP Conf. Ser. Mater. Sc. Eng.* **2018**, 324, 012049. [CrossRef]

**Disclaimer/Publisher's Note:** The statements, opinions and data contained in all publications are solely those of the individual author(s) and contributor(s) and not of MDPI and/or the editor(s). MDPI and/or the editor(s) disclaim responsibility for any injury to people or property resulting from any ideas, methods, instructions or products referred to in the content.